

Diese Arbeit wurde vorgelegt am Aerodynamischen Institut

# Investigations on two-way coupling effects of particle-laden decaying isotropic turbulent flows

---

PROJEKTARBEIT  
VON  
JULIAN STEMMERMAN, STEFFEN TRIENEKENS  
UND CHRISTIAN SOIKA

---

Aerodynamisches Institut der RWTH Aachen

8. Januar 2018

Betreuer: Konstantin Fröhlich

Erstprüfer: Univ.-Prof. Dr.-Ing. Wolfgang Schröder

# Contents

|          |   |           |
|----------|---|-----------|
| <b>I</b> | <b>Nomenclature</b>                               | <b>I</b>  |
| <b>1</b> | <b>Introduction</b>                               | <b>1</b>  |
| <b>2</b> | <b>Mathematical models</b>                        | <b>3</b>  |
| 2.1      | Equations governing the fluid phase . . . . .     | 3         |
| 2.2      | Scales of turbulent flows . . . . .               | 4         |
| 2.3      | Particle dynamics . . . . .                       | 5         |
| <b>3</b> | <b>Numerical methods</b>                          | <b>7</b>  |
| 3.1      | Discretization of the particle dynamics . . . . . | 7         |
| 3.2      | Direct numerical simulation . . . . .             | 8         |
| 3.3      | Large-eddy simulation . . . . .                   | 8         |
| <b>4</b> | <b>Results</b>                                    | <b>10</b> |
| 4.1      | Turbulence modulation by particles . . . . .      | 10        |
| 4.2      | Simulation setup . . . . .                        | 11        |
| 4.3      | Simulation results . . . . .                      | 11        |
| <b>5</b> | <b>Conclusion and outlook</b>                     | <b>16</b> |
| <b>6</b> | <b>References</b>                                 | <b>17</b> |
| <b>7</b> | <b>Appendix</b>                                   | <b>19</b> |

# I Nomenclature

## Acronyms

|      |                                |
|------|--------------------------------|
| CPP  | computational point particles  |
| DNS  | direct numerical simulation    |
| ILES | implicit large-eddy simulation |
| LES  | large-eddy simulation          |
| PP   | particle-laden simulation      |
| rms  | root mean square               |
| sgs  | subgrid scale                  |
| sP   | single-phase simulation        |

## Greek Symbols

|                     |   |
|---------------------|---|
| $\gamma$            | isentropic exponent   |
| $\Delta$            | cell length   |
| $\varepsilon$       | viscous dissipation rate  |
| $\varepsilon'$      | integral particle-induced dissipation rate  |
| $\bar{\varepsilon}$ | integral dissipation rate of the background flow field                                |
| $\eta$              | Kolmogorov length scale   |
| $\lambda$           | Taylor microscale   |
| $\lambda_c$         | ratio of physical point particles to computational point particles                    |
| $\mu$               | dynamic viscosity   |
| $\nu$               | kinematic viscosity   |
| $\rho$              | fluid density   |
| $\rho_p$            | particle density  |
| $\sigma$            | smoothing parameter   |
| $\bar{\tau}$        | stress tensor   |
| $\tau_\eta$         | Kolmogorov time scale   |
| $\tau_L$            | eddy turnover time  |
| $\tau_p$            | particle relaxation time  |
| $\Upsilon_f$        | fluid domain without particle surroundings  |
| $\phi(Re_p)$        | empirical drag correction factor as a function of the particle Reynolds number $Re_p$ |
| $\phi_m$            | mass fraction   |
| $\phi_v$            | volume fraction   |
| $\Psi$              | integral coupling rate  |
| $\Psi_p$            | coupling rate for one particle  |
| $\Psi_{pp}$         | integral coupling rate using the point-particle approach                              |
| $\Omega_p$          | vorticity vector of the undisturbed flow around one particle                          |

$\omega_p$  particle angular velocity vector

### Operators

$\frac{D}{Dt}$  time derivative following a fluid unit

$\frac{d}{dt}$  material derivative

$\delta t$  time step

$\frac{\partial}{\partial t}$  partial derivative with respect to time

$\nabla$  nabla operator

$:$  inner tensor product

### Roman Symbols

$A$  control surface

$\mathbf{a}_p$  particle acceleration

$c_p$  specific isobaric heat capacity

$c_v$  specific isochoric heat capacity

$d_i$  distance between particle position and cell center

$d_p$  particle diameter

$E$  specific inner energy

$E_k$  turbulent kinetic energy of the fluid

$E_{kB}$  mean kinetic energy of the particles

$\mathbf{e}$  unit vector in the same direction as  $\mathbf{u}'$

$e$  specific internal energy

$\mathbf{F}$  force vector per unit volume of the particle acting on the fluid

$\mathbf{F}_p$  force vector acting on the particles

$\mathbf{F}_{pp}$  force vector acting on the point-particles

$G(r)$  homogeneous filter function

$\bar{\mathbf{H}}$  flux tensor

$\bar{\mathbf{H}}^i$  inviscid part of the flux tensor

$\bar{\mathbf{H}}^v$  viscous part of the flux tensor

$\bar{\mathbf{I}}$  identity tensor

$K(t)$  history kernel

$k_t$  thermal conductivity

$L$  integral length scale

$l$  length

$m_f$  fluid mass

$m_p$  mass of one particle

$m_v$  mass of one cell

$N_c$  number of computational point particles

$N_p$  number of physical point particles

$\mathbf{n}$  normal vector

|                       |  |
|-----------------------|--|
| $p$                   | pressure   |
| $Pr$                  | Prandtl number   |
| $\mathbf{Q}$          | vector of conservative Eulerian variables                            |
| $\mathbf{q}$          | heat conduction vector   |
| $R$                   | specific gas constant  |
| $R(r, t)$             | two-point correlation as a function of the distance $r$ and time $t$ |
| $Re$                  | Reynolds number  |
| $Re_L$                | Reynolds number for the integral scale                               |
| $Re_p$                | particle Reynolds number   |
| $Re_\lambda$          | Taylor-scale Reynolds number   |
| $S$                   | Sutherland temperature   |
| $\bar{\mathbf{S}}$    | rate-of-strain tensor  |
| $T$                   | temperature  |
| $\mathbf{T}_p$        | particle torque vector   |
| $t$                   | time   |
| $t^*$                 | time normalized by initial eddy turnover time                        |
| $U$                   | characteristic fluid velocity  |
| $\bar{U}(\mathbf{x})$ | filtered velocity field  |
| $\mathbf{u}$          | fluid velocity vector  |
| $\mathbf{u}'$         | vector of fluid velocity fluctuations                                |
| $\mathbf{u}_p$        | vector of the undisturbed fluid velocity at the particle position    |
| $V$                   | control volume   |
| $V_f$                 | fluid volume   |
| $V_p$                 | particle volume  |
| $\mathbf{v}_p$        | particle velocity vector   |
| $\mathbf{x}$          | position vector  |
| $\mathbf{x}_p$        | particle position vector   |

### Subscripts

|          |                                  |
|----------|----------------------------------|
| $\infty$ | freestream value                 |
| $n$      | variable at $n$ -th timestep     |
| $n + 1$  | variable at $(n+1)$ -th timestep |
| ref      | reference value                  |
| 0        | initial values of the variable   |

# 1 Introduction

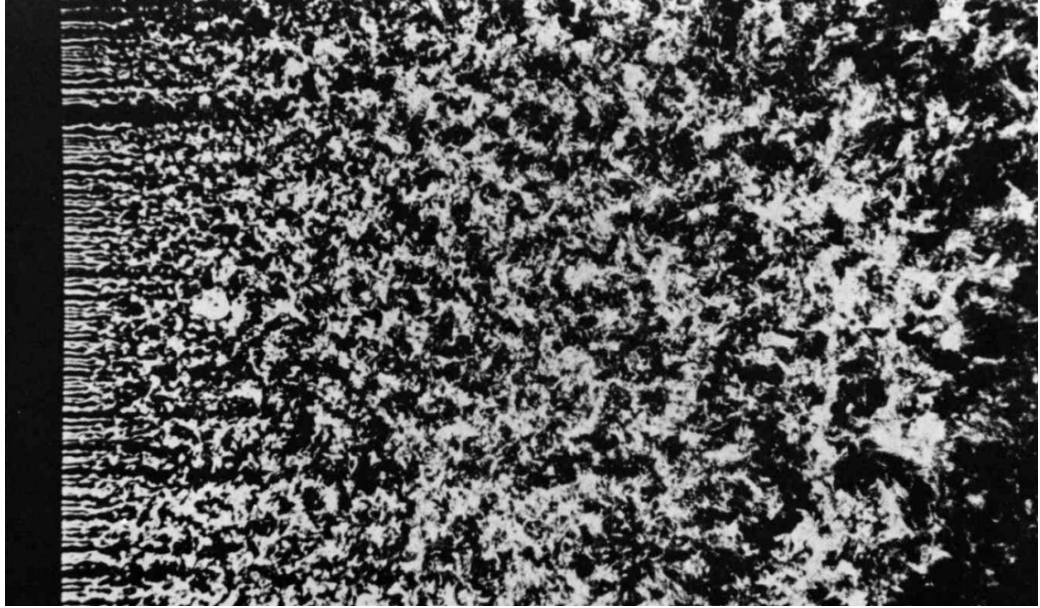


Figure 1. Formation of a locally homogeneous turbulent flow field behind a grid [23]. An isotropic decaying turbulence can be observed in a snapshot of the flow field moving with the mean flow.

Particle-laden turbulent flows are ubiquitous in nature. Spray atomization in fuel injectors, cyclonic particle separation in oil refineries, and sediment accumulation in pipelines are examples for technical applications, where it is of huge interest to predict the impact of the particles on turbulent flows. Turbulence augmentation or attenuation by particles is therefore a decisive factor.

A study about the impact of particles on the isotropic decaying turbulent flow is presented. Incompressible, isothermal, and isotropic decaying turbulence will serve as the carrier flow. Gravity is omitted to avoid prominent directions. Isotropic turbulence is a relatively good assumption for a small region with a high Reynolds number, which is not affected by boundary effects [9]. This concept is visualized in Fig. 1. Describing turbulent flows is a difficult task because of the presence of many different scales.

In this work the influence of the particles on the isotropic decaying turbulence is numerically analyzed by using direct numerical simulation (DNS) and large-eddy simulation (LES). DNS is able to resolve all scales of turbulent motion due to its high resolution. LES has a lower grid resolution and uses therefore a subgrid-scale (sgs) model for these scales. This type of simulation requires therefore less computational effort.

The simulations are carried out using the point-particle model, at which each

particle is tracked via a Lagrangian approach. The feedback of the particles on the flow field is modeled by sources and sinks, which is referred to as two-way coupling. Alternatives are one-way coupling, at which only the flow exerts influence on the particles, and four-way coupling, which extends two-way coupling by particle-particle interactions. Two-way coupling is fitting for the simulations in this study, because the volume fraction  $\phi_v = 10^{-3}$  of the particles is large enough to alter the turbulence. Volume fractions below  $\phi_v = 10^{-6}$  are referred to as one-way coupling and the interactions that can be observed at values greater than  $\phi_v = 10^{-3}$  are attributed to four-way coupling [17,18]. The particle diameter is defined to be smaller than the Kolmogorov scale, i.e., the smallest scale of the turbulent flow. The particle density is much higher than the fluid density.

To lower the computational effort in general, a new variable, which describes the fraction of physical to numerical point particles, is introduced and validated.

In the following, the structure of this work is described. First, mathematical models for single-phase flows and particle dynamics are given. Additionally, the scales of turbulent motion are introduced. Subsequently, the used discretization method to integrate the particle tracking equations is described and the 'computational point particles', in the following referred to as CPP, are introduced. Thereafter, the computational basics of both DNS and LES as well as their respective advantages and disadvantages are explained. The CPP approach is validated via turbulent kinetic energy budgets for LES and DNS. Finally, a short conclusion is given.

## 2 Mathematical models

In this section, the Navier-Stokes equations in integral formulation, the characteristic turbulent scales, and the kinematic and dynamic equations for the particle phase are introduced.

### 2.1 Equations governing the fluid phase

The conservation of mass, momentum, and energy for a control volume  $V$  reads

$$\int_V \frac{\partial \mathbf{Q}}{\partial t} dV + \int_{\partial V} \bar{\mathbf{H}} \cdot \mathbf{n} dA = \mathbf{0}, \quad (2.1)$$

with the time  $t$  and the flux tensor  $\bar{\mathbf{H}}$ . The vector  $\mathbf{Q}$  contains the fluid density  $\rho$ , fluid velocity  $\mathbf{u}$ , and specific inner energy  $E$ , with

$$\mathbf{Q} = \begin{pmatrix} \rho \\ \rho \mathbf{u} \\ \rho E \end{pmatrix}. \quad (2.2)$$

The flux tensor  $\bar{\mathbf{H}}$  contains the inviscid and viscous flux, i.e.

$$\bar{\mathbf{H}} = \bar{\mathbf{H}}^i + \bar{\mathbf{H}}^v = \begin{pmatrix} \rho \mathbf{u} \\ \rho \mathbf{u} \mathbf{u} + p \\ \mathbf{u}(\rho E + p) \end{pmatrix} - \frac{1}{Re} \begin{pmatrix} 0 \\ \bar{\boldsymbol{\tau}} \\ \bar{\boldsymbol{\tau}} \mathbf{u} + \mathbf{q} \end{pmatrix}, \quad (2.3)$$

with the shear stress  $\bar{\boldsymbol{\tau}}$ , heat conduction  $\mathbf{q}$ , and the pressure  $p$ . The Reynolds number  $Re = \frac{\rho_\infty u_\infty l_{\text{ref}}}{\mu_\infty}$  is defined to be the ratio of inertia forces to viscous forces with reference density  $\rho_\infty$ , velocity  $u_\infty$ , length  $l_{\text{ref}}$  and dynamic viscosity  $\mu_\infty$ .

The specific inner energy  $E$  and the heat conduction  $\mathbf{q}$  are defined as

$$E = e \frac{1}{2} |\mathbf{u}|^2, \quad (2.4)$$

and

$$\mathbf{q} = -\frac{\mu}{Pr(\gamma - 1)} \nabla T, \quad (2.5)$$

with the constant capacity ratio  $\gamma = \frac{c_p}{c_v}$  and the Prandtl number  $Pr = \frac{\mu_\infty c_p}{k_t}$  using the specific heat capacities of the fluid  $c_v$  and  $c_p$  and thermal conductivity  $k_t$ . Assuming that the fluid is newtonian, the Stokes hypothesis yields

$$\bar{\boldsymbol{\tau}} = 2\mu \bar{\mathbf{S}} - \frac{2}{3}\mu(\nabla \cdot \mathbf{u})\bar{\mathbf{I}}, \quad (2.6)$$



in which  $\bar{\mathbf{S}} = \frac{(\nabla \mathbf{u})(\nabla \mathbf{u})^T}{2}$  denotes the rate-of-strain tensor. Additionally, the viscosity  $\mu$  can be approximated by Sutherland's law

$$\mu(T) = \mu_\infty \left( \frac{T}{T_\infty} \right)^{3/2} \frac{T_\infty + S}{T + S}, \quad (2.7)$$

where  $S$  is the Sutherland temperature and  $T_\infty$  the reference temperature. To achieve closure the caloric state equation  $e = c_v T$  and the state equation for an ideal gas  $p = \rho R T$  are used. The specific gas constant is determined by  $R = c_p - c_v$ .

## 2.2 Scales of turbulent flows

Turbulent flows can be described as a superposition of chaotic, three-dimensional vortical structures of various scales, referred to as eddies. Larger eddies decay and pass their kinetic energy down to smaller scales. At the smallest scales, the kinetic energy finally dissipates into heat due to the viscous dissipation. This behavior is called the 'energy cascade' and was first described by Richardson [12] and quantified by Kolmogorov [9].

Considering homogeneous isotropic turbulence with zero mean velocity, the characteristic length scales of a turbulent flow can be defined by the two-point correlation  $R$ , which is the normalized product of the absolute value  $u'$  of the velocity fluctuation  $\mathbf{u}'$  at two different positions  $\mathbf{x}$  and  $\mathbf{x} + \mathbf{e}r$  at the same time  $t$

$$R(r, t) = \frac{\overline{u'(\mathbf{x}, t) u'(\mathbf{x} + \mathbf{e}r, t)}}{\overline{u'^2}}. \quad (2.8)$$

$\mathbf{e}$  points in the same direction as  $\mathbf{u}'$  with  $|\mathbf{e}| = 1$ . The Taylor microscale  $\lambda$  and the integral length scale  $L$  are defined by

$$\frac{1}{\lambda^2} = -\frac{1}{2} \left( \frac{\partial^2 R}{\partial r^2} \Big|_{r=0} \right) \quad (2.9)$$

and

$$L = \int_0^\infty R(r, t) \, dr. \quad (2.10)$$

The Taylor microscale and the root-mean-square velocity  $u_{\text{rms}}$  can be used to compute the Taylor-scale Reynolds number

$$Re_\lambda = \frac{u_{\text{rms}} \lambda}{\nu}. \quad (2.11)$$

The integral length scale  $L$  and the corresponding timescale  $\tau_L$ , which is mostly

called eddy turnover time, describe the large eddies. At these scales the energy is brought into the flow, creating the energy-containing range. The eddy turnover time is defined by

$$\tau_L = \frac{L}{u_{\text{rms}}}. \quad (2.12)$$

The smallest scales in a turbulent flow are the Kolmogorov length  $\eta$  and time scale  $\tau_\eta$ . At these scales, the effects of viscosity take place and the energy dissipates into heat. With the estimate of the viscous dissipation rate  $\varepsilon = \mathcal{O}\left(\frac{u_{\text{rms}}^3}{L}\right)$  they can be written as

$$\eta = \mathcal{O}\left(\left(\frac{\nu^3 L}{u_{\text{rms}}^3}\right)^{1/4}\right) \quad (2.13)$$

and

$$\tau_\eta = \mathcal{O}\left(\frac{\nu L}{u_{\text{rms}}^3}\right). \quad (2.14)$$

Both these scales are coupled by the Reynolds number

$$\frac{L}{\eta} = \mathcal{O}\left(Re_L^{3/4}\right) \quad (2.15)$$

and

$$\frac{\tau_L}{\tau_\eta} = \mathcal{O}\left(Re_L^{1/2}\right) \quad (2.16)$$

with  $Re_L = \frac{u' L}{\nu}$ . It can be observed from these equations that the range between the scales increases for higher Reynolds numbers.

### 2.3 Particle dynamics

The sum of several pressure and shear forces acting on the particles is described by the Maxey-Riley equation [14]. Reduced to the governing forces and with neglect of gravity the force  $\mathbf{F}_{\text{pp}}$  acting on the particles reads

$$\begin{aligned} \mathbf{F}_{\text{pp}} = m_p \frac{d\mathbf{v}_p}{dt} = \rho V_p \frac{D\mathbf{u}_p}{Dt} + 3\pi\mu d_p (\mathbf{u}_p - \mathbf{v}_p) \phi(Re_p) + \frac{1}{2}\rho V_p \left( \frac{D\mathbf{u}_p}{Dt} - \frac{d\mathbf{v}_p}{dt} \right) + \\ 3\pi\mu d_p \int_0^t K(t)(t-t') \cdot \left( \frac{d\mathbf{u}_p}{dt'} - \frac{d\mathbf{v}_p}{dt'} \right) dt'. \end{aligned} \quad (2.17)$$

$\mathbf{v}_p(\mathbf{x}_p, t)$  is the particle velocity vector with the time derivative  $\frac{d}{dt}$  along the particle trajectory, while  $\frac{D}{Dt}$  is the material derivative at one point.  $\mathbf{u}_p(\mathbf{x}_p, t)$  is the velocity of the undisturbed fluid at the particle position  $\mathbf{x}_p$ . The individual forces on the right side of the equation are stated in the following:

- $\rho V_p \frac{D\mathbf{u}_p}{Dt}$ :  
pressure gradient of the undisturbed flow

- $3\pi\mu d_p(\mathbf{u}_p - \mathbf{v}_p)\phi(Re_p)$  :  
quasi-steady Stokes drag, parallel to the undisturbed streamlines, which is described by the Stokes' law as the force acting on spherical particles at very low Reynolds numbers in viscous flows
- $\frac{1}{2}\rho V_p \left( \frac{D\mathbf{u}_p}{Dt} - \frac{d\mathbf{v}_p}{dt} \right)$  :  
added mass force, which represents the influence of the fluid's inertia in case of a different acceleration compared to the particles
- $3\pi\mu d_p \int_0^t K(t)(t - t') \cdot \left( \frac{d\mathbf{u}_p}{dt'} - \frac{d\mathbf{v}_p}{dt'} \right) dt'$  :  
Basset history force taking the unsteady motion into account using a history kernel  $K(t)$

Equation (2.17) is based on Stokes flow conditions, i.e., vanishing particle Reynolds number  $Re_p \ll 1$ , and in general only valid for particles with  $d_p \ll \eta$ . For heavy particles, the drag force is the dominating contributor of Eq. (2.17) as reported in [22]. Therefore  $\mathbf{F}_{pp}$  can be reduced to

$$\mathbf{F}_{pp} = m_p \frac{d\mathbf{v}_p}{dt} = 3\pi\mu d_p(\mathbf{u}_p - \mathbf{v}_p)\phi(Re_p). \quad (2.18)$$

The empirical correction factor  $\phi(Re_p) = 1 + 0.15Re_p^{0.687}$  is used for finite  $Re_p$ . Eq. (2.18) can be reformulated to

$$\frac{d\mathbf{v}_p}{dt} = \frac{\phi(Re_p)}{\tau_p}(\mathbf{u}_p - \mathbf{v}_p), \quad (2.19)$$

with the particle relaxation time  $\tau_p = \frac{1}{18} \frac{\rho_p}{\rho} \frac{d_p^2}{\nu}$ .

Together with the kinematic equation

$$\frac{d\mathbf{x}_p}{dt} = \mathbf{v}_p, \quad (2.20)$$

the Eqs. (2.1) and (2.18) form a closed system of equations.

### 3 Numerical methods

Two numerical methods, DNS and LES, are discussed and their main differences are pointed out in the following chapter. The basis of both are the Navier-Stokes equations as described above. The simulations were carried out using ZFS, the simulation tool developed and implemented at the Institute of Aerodynamics at RWTH Aachen University [4, 5]. The tool is capable of simulating compressible finite-volume flows using unstructured Cartesian grids.

#### 3.1 Discretization of the particle dynamics

To compute the Lagrangian particle trajectories, a predictor-corrector scheme based on the trapezoidal rule for numerical integration

$$f(t + \delta t) \approx f(t) + \frac{\delta t}{2} \left[ \frac{\partial f(t)}{\partial t} + \frac{\partial f(t + \delta t)}{\partial t} \right] \quad (3.1)$$

is used.

The first step is the prediction of the new particle position  $\mathbf{x}_{p,n+1}$  using a Taylor expansion for a small time step  $\delta t$

$$\mathbf{x}_{p,n+1} = \mathbf{x}_{p,n} + \delta t \mathbf{v}_{p,n} + \frac{1}{2} \delta t^2 \mathbf{a}_{p,n}, \quad (3.2)$$

with  $\mathbf{a}_{p,n}$  being the particle acceleration, where the subscript  $p$  denotes the particle and the subscript  $n$  the time step. To avoid filtering effects, the fluid velocity  $\mathbf{u}_{p,n+1}$  at the particle position  $\mathbf{x}_{p,n+1}$  is set equal to the nearest cell fluid velocity. The predicted velocity and acceleration are calculated with

$$\mathbf{v}_{p,n+1} = \frac{\mathbf{v}_{p,n} + \frac{1}{2} \delta t \left( \mathbf{a}_{p,n} + \frac{\phi(Re_p)}{\tau_p} \mathbf{u}_{p,n+1} \right)}{1 + \frac{1}{2} \frac{\phi(Re_p)}{\tau_p} \delta t}, \quad (3.3)$$

$$\mathbf{a}_{p,n+1} = \frac{\frac{\phi(Re_p)}{\tau_p} (\mathbf{u}_{p,n+1} - \mathbf{v}_{p,n} - \frac{1}{2} \delta t \mathbf{a}_{p,n})}{1 + \frac{1}{2} \frac{\phi(Re_p)}{\tau_p} \delta t}. \quad (3.4)$$

The updated particle position must be corrected by an additional term according to the trapezoidal rule

$$\mathbf{x}_{p,n+1} = \mathbf{x}_{p,n} + \frac{1}{2} \delta t (\mathbf{v}_{p,n+1} + \mathbf{v}_{p,n}) + \frac{1}{12} \delta t^2 (\mathbf{a}_{p,n+1} - \mathbf{a}_{p,n}). \quad (3.5)$$

These approaches to compute the particle trajectories require a lot of computational resources.

To reduce these requirements the creation of numerical clusters of point particles is considered. For this purpose the ratio  $\lambda_c$  of physical point particles  $N_p$  to CPPs  $N_c$  is introduced ( $\lambda_c = \frac{N_p}{N_c}$ ). To compensate this lack of particles, the feedback force is multiplied by  $\lambda_c$ , due to the  $\lambda_c$ -fold mass of the (cluster-)particles.

To model the impact of the particles on the fluid, the Navier-Stokes equations (2.1) are extended by momentum sources or sinks. The feedback force of the particles  $\mathbf{F}$  is exerted on the fluid using a distance based weighting function

$$\mathbf{F}_i = \mathbf{F}_{pp} \cdot \frac{e^{-(d_i^2/(\sigma\Delta^2))}}{\sum_i e^{-(d_i^2/(\sigma\Delta^2))}}, \quad (3.6)$$

with  $d_i$  being the distance between particle position and the center of the cell  $i$ , the grid width  $\Delta$ , and a smoothing parameter  $\sigma$  that controls the distribution of  $\mathbf{F}$  on the adjacent cells.

### 3.2 Direct numerical simulation

With DNS, the Navier-Stokes equations are solved completely. This provides a very accurate result, as all scales of motion are being resolved. However, it requires an immense level of computational resources which increase exponentially with the Reynolds number. With the LES, as described below, the computational effort is 99.98 % less compared to DNS, which is the fraction of the dissipative scale. This leaves 0.02 % of the flow, which is correlative with the fraction of the energy-containing large scales [16].

### 3.3 Large-eddy simulation

Due to the fact that DNS is effortful, LES was established to save time and resources. The energy-containing large scales are completely resolved and the impact of the small scales on the large scales are modeled.

Simulating only the large-scale motions is called filtering, which means that the small-scale motions, also known as fluctuation, are filtered out. The filtered velocity field is calculated by

$$\bar{U}(\mathbf{x}) = \int_{-\infty}^{\infty} G(\mathbf{r})U(\mathbf{x} - \mathbf{r}) d\mathbf{r}, \quad (3.7)$$

with  $G(\mathbf{r})$  being a homogeneous filter function [16]. To model the filtered smaller-scale motions an sgs model is necessary. According to Hickel [20] the interference

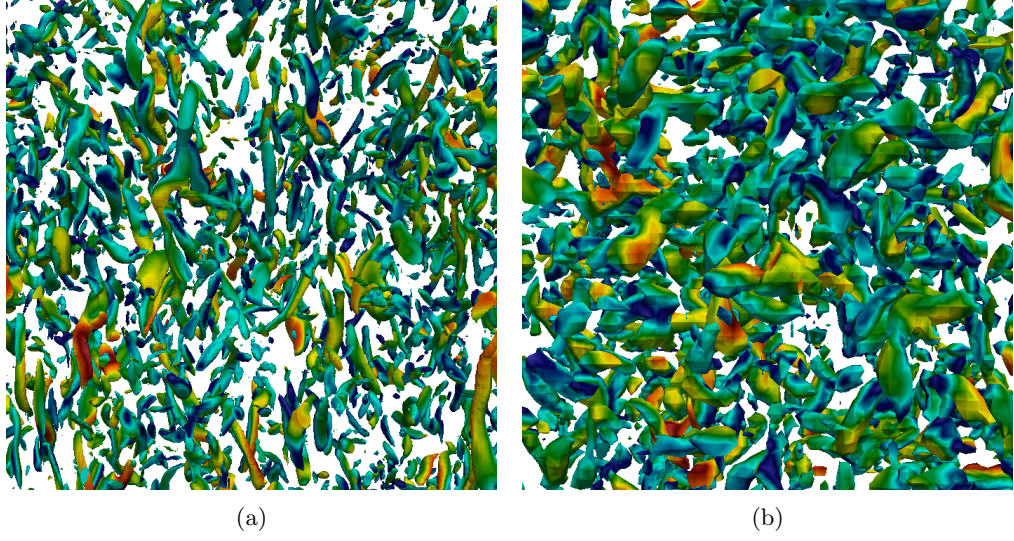


Figure 2. Instantaneous snapshot of the parallel projection of an isotropic decaying turbulent flow field computed by a DNS (a) and an LES (b). The DNS requires  $256^3$  cells, whereas the LES employed  $64^3$  cells. 'Worm-like' structures in an isotropic turbulent flow field can be observed. The more refined grid on the left shows more and better resolved structures, while the right picture reveals more artificially generated artifacts. For details on creation, see Appendix.

between explicit sgs and the truncation error can be exploited, i.e., the truncation error can serve as model of the effects of the unresolved scales, which is therefore an implicit sgs model. Thus it is called implicit LES (ILES).

Even though the small scales are modeled in the LES, the effects of filtering can be observed in Fig. 2.

## 4 Results

In this section, the setup and the results of the DNS and LES of particle-laden decaying isotropic turbulence will be presented. Special emphasis will be put on the analysis of the turbulent kinetic energy budgets.

### 4.1 Turbulence modulation by particles

The turbulence modulation by particles in particle-laden decaying isotropic turbulence is determined by the coupling rate  $\Psi$ , which describes the energy transfer between the fluid and the particle phase, by the background dissipation rate of the flow field  $\bar{\varepsilon}$  and by the particle-induced dissipation rate  $\varepsilon'$ . These contributions form an equation, which describes the change in turbulent kinetic energy

$$\frac{dE_k}{dt} = \Psi(t) - \bar{\varepsilon}(t) - \varepsilon'(t). \quad (4.1)$$

As the dissipation rate is always of positive value, it acts as a sink for the turbulent kinetic energy. In contrast to that, the coupling rate can serve either as source or sink depending on the acceleration of the particles [11]. The coupling rate for fully resolved particles  $\Psi$  is defined as

$$\Psi(t) = \sum_{p=1}^{N_p} \Psi_p = - \sum_{p=1}^{N_p} (\mathbf{F}_p \cdot \mathbf{v}_p + \mathbf{T}_p \cdot \boldsymbol{\omega}_p), \quad (4.2)$$

using surface force  $\mathbf{F}_p$ , particle velocity  $\mathbf{v}_p$ , torque  $\mathbf{T}_p$  and angular velocity  $\boldsymbol{\omega}_p$  to describe the transfer of kinetic energy resulting at each particle.

As mentioned before, the flow field is considered nearly incompressible, therefore the equation for the viscous dissipation rate can be approximated by

$$\varepsilon(t) \approx 2\mu \bar{\mathbf{S}} : \bar{\mathbf{S}}, \quad (4.3)$$

where  $:$  denotes the inner tensor product. This rate can then be integrated over the fluid domain excluding particles and their direct surroundings  $\Upsilon_f$ , which leads to the background dissipation rate

$$\bar{\varepsilon}(t) = \int_{\Upsilon_f} \varepsilon(t) dV. \quad (4.4)$$

Additionally, the particles change the fluid's rate of dissipation due to their volume forces. Neglecting fluid inertia forces, the additional dissipation rate for fully resolved particles can be computed by

$$\varepsilon' = \sum_{p=1}^{N_p} \mathbf{F}_p \cdot (\mathbf{u}_p - \mathbf{v}_p) + \mathbf{T}_p \cdot (\boldsymbol{\Omega}_p - \boldsymbol{\omega}_p), \quad \rho_p \gg \rho, \quad (4.5)$$

using the vorticity vector of the undisturbed flow around one particle  $\boldsymbol{\Omega}_p$  at the particle position.

For  $\rho_p \gg \rho$ , and the point-particle approach the coupling rate  $\Psi$  and the additional dissipation rate  $\varepsilon'$  are implicitly coupled. Torque and angular velocity were neglected for the point-particle approach and  $\mathbf{F}_{pp}$  is modeled with Eq. 2.18, which leads to

$$\Psi_{pp}(t) = \Psi - \varepsilon'(t) = - \sum_{p=1}^{N_p} \mathbf{F}_{pp} \cdot \mathbf{u}_p. \quad (4.6)$$

Therefore, the turbulent kinetic energy budget for the point-particle approach reads

$$\frac{dE_k}{dt} = \Psi_{pp}(t) - \bar{\varepsilon}(t) = - \sum_{p=1}^{N_p} \mathbf{F}_{pp} \cdot \mathbf{u}_p - \bar{\varepsilon}(t). \quad (4.7)$$

## 4.2 Simulation setup

All cases were simulated on a cubic domain and a Cartesian grid using different grid refinement levels. For the LES cases  $64^3$ ,  $96^3$  and  $128^3$  cells are employed, which have been already validated in [8]. For a DNS,  $256^3$  cells are necessary to resolve all scales.

The particle-free case was initialized using a seed-based random number generator, which is described in detail in [21]. At  $t^* = t \frac{\varepsilon_0}{u_{rms,0}^2} \approx 0.27 = t_{inj}^*$ , where  $t^*$  is the time normalized by the initial viscous dissipation rate  $\varepsilon_0$  and initial rms-velocity  $u_{rms,0}$ , a restart file is written out to initialize the subsequent simulation of the particle-laden isotropic turbulence.

The single-phase DNS and particle-laden DNS will be used as reference for analyzing other results. The single-phase results will be in the following referred to as sP, and particle-laden results as PP. The PP simulations are set up to match the volume fraction  $\phi_v = \frac{V_p}{V_f} = 10^{-3}$  and mass fraction of  $\phi_m = \frac{m_p}{m_f} = 1$ . Hence, the density ratio is  $\frac{\rho_p}{\rho} = 1000$  and the particle diameter is  $d_p \approx 0.6\eta_0$  with  $\eta_0$  being the initial Kolmogorov length. At the time step of the injection, the Taylor Reynolds number is  $Re_\lambda \approx 58$ .

## 4.3 Simulation results

At first, a test is required to investigate the number of particles needed to achieve approximately converged statistics. Figure 3 therefore shows the relative deviation



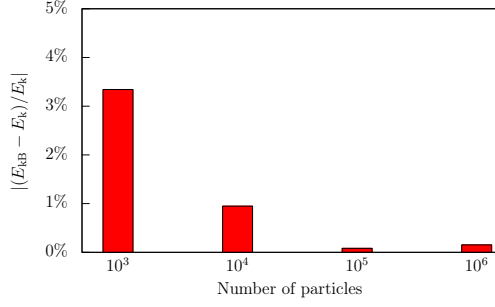


Figure 3. Relative deviation of the kinetic energy of the particles  $E_{kB}$  from the turbulent kinetic energy  $E_k$  at  $t_{inj}^*$  for an PP-LES<sub>128</sub>. An inaccuracy can be observed for small numbers of particles. This behavior can be noticed for all other resolutions. The relative deviation of the particles' kinetic energy and the turbulent kinetic energy is below 1% for more than  $10^4$  particles.

of the particles' kinetic energy  $E_{kB}$  from the turbulent kinetic energy  $E_k$  at injection time  $t_{inj}^*$  for different numbers of particles. For higher numbers of particles the deviation decreases. For  $10^4$  particles the deviation is below 1%. This leads to the assumption that simulations with a  $\lambda_c$  of 100 seem fitting with an overall number of  $10^6$  particles. To investigate the influence of CPPs on the accuracy of

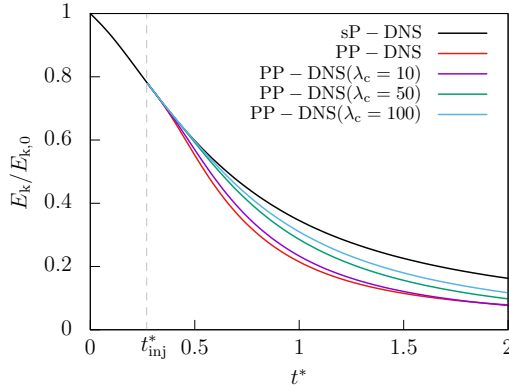


Figure 4. Temporal development of the kinetic energy  $E_k$  normalized by its initial value  $E_{k,0}$ . Shortly after the injection, the PP-cases separate from the sP-flow. The higher-clustered cases show significant differences compared to the unclustered reference case

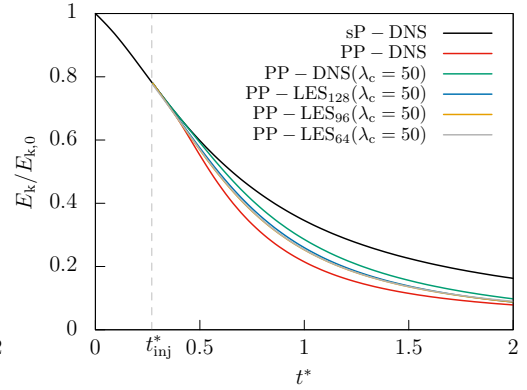


Figure 5. Temporal development of the kinetic energy  $E_k$  normalized by its initial value  $E_{k,0}$  for different grid resolutions and with constant  $\lambda_c = 50$ . The results of the less resolved cases are more similar to the particle-laden reference case PP-DNS.

the simulations, the variable  $\lambda_c$ , introduced in Sec. 3.1, was implemented in the program code. All simulations were then set up with the overall same number of  $10^6$  particles, and  $\lambda_c$  was set to 10, 50 and 100. Additionally, simulations of the single-phase flow and an unclustered particle-laden flow were conducted.

Figure 4 shows the evolution of the turbulent kinetic energy  $E_k$  normalized by the initial turbulent kinetic Energy  $E_{k,0}$  in time of the DNS using different  $\lambda_c$  and constant grid resolution. Shortly after injection, the number of clustered particles has a high impact on the turbulent kinetic energy. For increasing  $\lambda_c$ , the turbu-

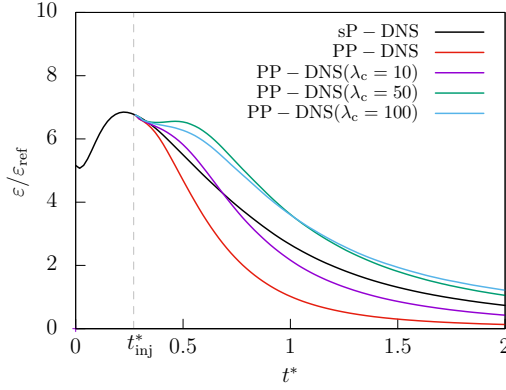


Figure 6. Temporal development of the normalized dissipation rate  $\varepsilon$ . The unclustered PP-case shows a lower dissipation rate than the sP-case. Highly clustered PP-cases show a higher dissipation rate.

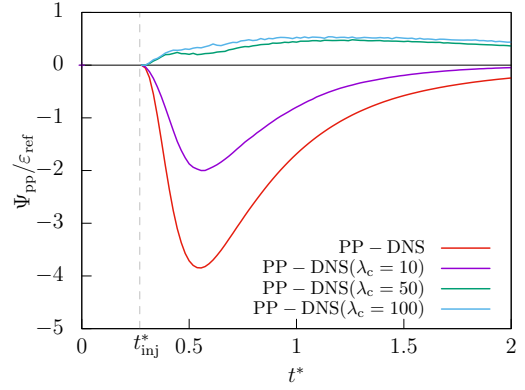


Figure 7. Temporal development of the normalized point-particle coupling rate  $\Psi_{pp}$ . The PP-case without clustering shows the lowest coupling rate. Both highly-clustered PP-cases show positive contribution in contrast to the reference case PP-DNS.

lence attenuation by particles is underpredicted. The behavior of lower-resolution particle-laden simulations seems to be less prone to CPPs as can be observed in Fig. 5. The same variables are displayed as in Fig. 4 for constant  $\lambda_c = 50$  and varying grid resolutions. The coarser simulations are closer to the PP-DNS reference as the higher resolved simulations. It can be observed that both the CPPs and the grid refinement level have an impact on the accuracy of the simulation. Therefore, further investigations on the reasons of this behavior will follow. The development of the normalized dissipation rate  $\varepsilon$  is displayed in Fig. 6, showing a lower rate for the unclustered PP-DNS and a higher rate for the higher-clustered PP-DNS cases in comparison to the single-phase simulation.

Figure 7 shows the temporal development of the point-particle coupling rate  $\Psi_{pp}$ . Similar to Fig. 6, the PP-DNS with a high  $\lambda_c$  show larger deviation from the PP-DNS reference, leading to a positive coupling rate for  $\lambda_c \geq 50$ . Both these figures can be analyzed using the turbulent kinetic energy budget introduced in Sec. 4.1.

The variables of the PP-DNS and PP-LES<sub>64</sub> at  $t^* = 1$  can be found in Tab. 1. A correlation between less accurate results and higher ratios of mass of a particle cluster  $m_c$  to the fluid mass of one cell  $m_v$  can be observed. Since the PP-LES<sub>64</sub> is not fine enough to resolve the smaller scales, the viscous dissipation rate  $\varepsilon$ , the Taylor microscale  $\lambda$  and the Kolmogorov length  $\eta$  are not displayed in the table. The simulation on a  $64^3$ -grid is therefore less prone to the modeling error of the CPPs, because the cells and therefore the fluid mass of one cell, are substantially bigger than in the  $256^3$ -grid. It seems to be the case that for increasing mass ratio

| Case                 | $\lambda_c$ | $\frac{m_c}{m_v}$ | $\varepsilon \frac{L}{u_{\text{rms},0}^3}$ | $\frac{\lambda}{L}$ | $\frac{\eta}{L}$ | $Re_\lambda$ | $\frac{E_k}{E_{k,0}}$ | $\frac{E_{kB}}{E_{k,0}}$ |
|----------------------|-------------|-------------------|--|---------------------|------------------|--------------|-----------------------|--------------------------|
| PP-DNS               | 1           | 16.78             | 0.97                                       | 0.039               | 0.0032           | 38.73        | 0.21                  | 0.29                     |
|                      | 10          | 167.78            | 2.08                                       | 0.028               | 0.0026           | 28.66        | 0.23                  | 0.34                     |
|                      | 50          | 838.86            | 3.51                                       | 0.024               | 0.0023           | 27.31        | 0.28                  | 0.52                     |
|                      | 100         | 1677.72           | 3.51                                       | 0.025               | 0.0023           | 29.42        | 0.31                  | 0.62                     |
| PP-LES <sub>64</sub> | 1           | 0.26              |  |                     |                  | 48.26        | 0.23                  | 0.28                     |
|                      | 10          | 2.62              |  |                     |                  | 48.13        | 0.23                  | 0.28                     |
|                      | 50          | 13.11             |  |                     |                  | 47.54        | 0.25                  | 0.30                     |
|                      | 100         | 26.21             |  |                     |                  | 47.60        | 0.27                  | 0.30                     |

Table 1. Non-dimensional variables of the simulations at  $t^* = 1$  of the PP-DNS and the PP-LES<sub>64</sub>: Ratio of physical to computational point-particles  $\lambda_c$ , fraction of mass of one cluster  $m_c$  to the fluid mass of one cell  $m_v$ , viscous dissipation rate  $\varepsilon$ , Taylor microscale  $\lambda$ , Kolmogorov length  $\eta$ , Taylor-scale Reynolds number  $Re_\lambda$ , kinetic energy of the fluid  $E_k$ , and kinetic energy of the particles  $E_{kB}$ . The dissipation rate, Taylor microscale, and Kolmogorov length are not resolved by the PP-LES<sub>64</sub>.

of one cluster to the fluid content of one cell the simulation results become less accurate. This phenomenon was first described in [15], as particle-induced point forces induce a vorticity to the flow at the particle position.

It has been shown in [10] that the PP-DNS correctly predicts the turbulence modulation. Higher grid refinement leads to better results, while higher mass fractions of particles to cells lead to less accurate results. Figure 8 shows the temporal development of the point-particle coupling rate  $\Psi_{pp}$  for different grid refinement levels. It can be observed that a correlation between the inaccuracy of the simu-

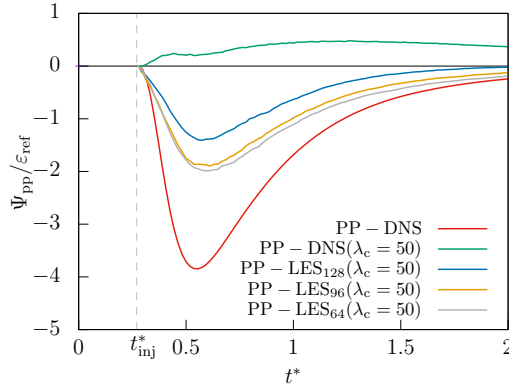


Figure 8. Temporal development of the point-particle coupling rate  $\Psi_{pp}$  normalized by  $\varepsilon_{\text{ref}}$  with constant  $\lambda_c$  for various resolutions. A correlation between the resolution and the accuracy can be observed.

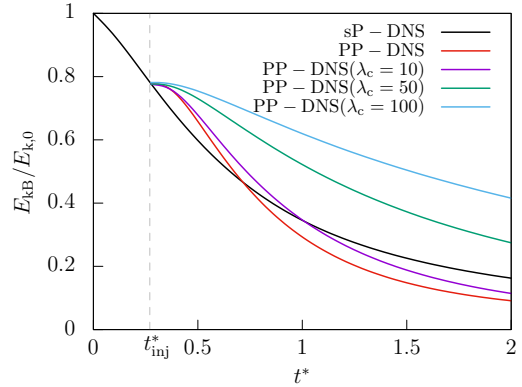


Figure 9. Temporal development of the kinetic energy of the particles  $E_{kB}$  normalized by initial turbulent kinetic energy. The PP-case without clustering shows the biggest decay of the kinetic energy.

lations and the refinement level of the grid exists. For the same ratio of physical to computational point particles, the results show different behavior depending on the grid refinement level. It is therefore less critical to cluster particles in lower-resolution grids, although the results are not nearly as accurate as for the unclustered simulations.

In Fig. 9, the development of the kinetic energy of the particles is displayed. For increasing  $\lambda_c$ , the kinetic energy of the particles becomes larger. This behavior leads to the assumption that the clustering produces the behavior of heavy particles comparable to [11].

## 5 Conclusion and outlook

In this study, various simulations of particle-laden isotropic turbulence are carried out to investigate the influence of CPPs on the simulation accuracy of a DNS and LES. A point-particle approach is used to simulate the two-way coupling of heavy particles and the surrounding fluid. The particle diameter is smaller than the Kolmogorov scale  $d_p < \eta$ . A DNS on a grid with  $256^3$  cells serves as reference for validation of the method of CPPs. CPPs are introduced in various numbers on multiple grid refinement levels. The concept of CPPs is object of this study because of the possible potential in lowering computational effort for future simulations. Therefore, the accuracy of the simulations is the critical criteria. The turbulent kinetic energy budget is investigated to analyze possible correlation of different variables and the influence of the grid refinement level and CPPs. In addition to the evolution of the kinetic energy, the point-particle coupling rate and the dissipation rate are evaluated.

A correlation between the ratio of the mass of one particle cluster to the fluid mass of a cell and the simulation's accuracy is found. With an increasing ratio, the simulations diverge from the reference case. This behavior is found for all resolutions. Additionally, the results of simulations with lower mass ratios do not necessarily converge towards the reference. It is likely, that the mass ratio is not the only parameter responsible for accurate or inaccurate results. Most probably, a combination of grid refinement and mass ratio is responsible for accuracy in the simulations. It is found that the behavior of particle clusters, as simulated in this work, shows similarities to heavy particles, as described in [11].

The method evaluated in this work seems to be less practical for these particle parameters. Nevertheless the method could be useful for smaller particles, which would have a smaller fraction of mass for the same number of particles simulated. Further investigation for the requirements for the specific mass fraction and grid refinement combination could be tested in the future to develop a catalog of mass fractions, grid refinement and the resulting accuracy for practical use in technical applications.

## Acknowledgements

We would like to thank Konstantin Fröhlich, who supervised this work. Thank you for the chance of learning about turbulent flows and simulations, the advice and the deep insights in scientific work. We also appreciate the opportunity of writing this work at the Institute of Aerodynamics of the RWTH Aachen University.

## 6 References

- [1] A. Ferrante and S. Elghobashi. On the physical mechanisms of two-way coupling in particle-laden isotropic turbulence. *Phys. Fluids*, 15(2):315–329, 2003.
- [2] A. Prosperetti and G. Tryggvason. *Computational methods for multiphase flow*. Cambridge University Press, 2009.
- [3] C. Siewert. *Numerical Analysis of Particle Collisions in Isotropic Turbulence*. PhD thesis, 2014.
- [4] D. Hartmann, M. Meinke and W. Schröder. An adaptive multilevel multi-grid formulation for Cartesian hierarchical grid methods. *Comput. Fluids*, 37(9):1103–1125, 2008.
- [5] D. Hartmann, M. Meinke and W. Schröder. A strictly conservative Cartesian cut-cell method for compressible viscous flows on adaptive grids. *Comput. Methods in Appl. Mech. Eng.*, 200(9):1038–1052, 2011.
- [6] J.R. Fessler, J.D. Kulick and J.K. Eaton. Preferential concentration of heavy particles in a turbulent channel flow. *Phys. Fluids*, 6(11):3742–3749, 1994.
- [7] K. Fröhlich, L. Schneiders, M. Meinke and W. Schröder. Validation of Lagrangian two-way coupled point-particle models in large-eddy simulations. *Submitted to Flow Turbul. Combust.*, 2017.
- [8] K. Fröhlich, L. Schneiders, M. Meinke and W. Schröder. Validation of Particle-Laden Large-Eddy Simulation Using HPC Systems. *Sustained Simulation Performance 2017*, 137–149. Springer, 2017.
- [9] A. N. Kolmogorov. The local structure of turbulence in incompressible viscous fluid for very large reynolds numbers. *Proc. Royal Soc. A*, 434(1890):9–13, 1991.
- [10] L. Schneiders, C. Günther, M. Meinke and W. Schröder. An efficient conservative cut-cell method for rigid bodies interacting with viscous compressible flows. *J. Comput. Phys.*, 311(Supplement C):62 – 86, 2016.
- [11] L. Schneiders, M. Meinke and W. Schröder. Direct particle–fluid simulation of kolmogorov-length-scale size particles in decaying isotropic turbulence. *J. Fluid Mech.*, 819:188–227, 2017.

- [12] L.F. Richardson. The supply of energy from and to atmospheric eddies. *Proc. Royal Soc. A*, 97(686):354–373, 1920.
- [13] M. Boivin, O. Simonin and K.D. Squires. Direct numerical simulation of turbulence modulation by particles in isotropic turbulence. *J. Fluid Mech.*, 375:235–263, 1998.
- [14] M.R. Maxey and J.J. Riley. Equation of motion for a small rigid sphere in a nonuniform flow. *Phys. Fluids*, 26(4):883–889, 1983.
- [15] M.R. Maxey, B.K. Patel, E.J. Chang and L.-P. Wang. Simulations of dispersed turbulent multiphase flow. *Fluid Dyn. Res.*, 20(1-6):143–156, 1997.
- [16] S. B. Pope. *Turbulent flows*. Cambridge University Press, 2000.
- [17] S. Elghobashi. Particle-laden turbulent flows: direct simulation and closure models. *Appl. Sci. Res.*, 48(3):301–314, 1991.
- [18] S. Elghobashi. On predicting particle-laden turbulent flows. *Appl. Sci. Res.*, 52(4):309–329, 1994.
- [19] S. Elghobashi and G.C. Truesdell. Direct simulation of particle dispersion in a decaying isotropic turbulence. *J. Fluid Mech.*, 242:655–700, 1992.
- [20] S. Hickel. *Implicit turbulence modeling for large-eddy simulation*. PhD thesis, 2008.
- [21] S.A. Orszag. Numerical methods for the simulation of turbulence. *Phys. Fluids*, 12(12):II–250, 1969.
- [22] V. Armenio and V. Fiorotto. The importance of the forces acting on particles in turbulent flows. *Phys. Fluids*, 13(8):2437–2440, 2001.
- [23] M. van Dyke. *An album of fluid motion*. Parabolic Press Stanford, 1982.

## 7 Appendix

### Creating of pictures showing tubular structures

The pictures used to point out the differences between DNS and LES were generated using ParaView, an open-source-software developed by a joint-venture of Kitware and the Los Alamos National Laboratory. More information about the software can be found at [www.paraview.org](http://www.paraview.org). To show the tubular structures in a turbulent flow, two filters were used: The AIALambda2Criterion1-Filter and the ISOVolume1-Filter. These filters were then set to visualize the velocity of the flow colored by magnitude. To diversify the different velocity magnitudes, a rainbow colorscheme was used.